Biosensors and Bioelectronics 86 (2016) 337–345

Contents lists available at ScienceDirect

Biosensors and Bioelectronics

journal homepage: www.elsevier.com/locate/bios

Ultrasensitive electrochemical sensing platform for microRNA based on tungsten oxide-graphene composites coupling with catalyzed hairpin assembly target recycling and enzyme signal amplification

Hong-Lei Shuai, Ke-Jing Huang*, Ling-Li Xing, Ying-Xu Chen

College of Chemistry and Chemical Engineering, Xinyang Normal University, Xinyang 464000, China

ARTICLE INFO

Article history:
Received 19 April 2016
Received in revised form
6 June 2016
Accepted 19 June 2016
Available online 23 June 2016

Keywords:
Tungsten oxide-graphene
Target recycling
miRNAs biosensing
Catalyzed hairpin assembly
Electrochemical-chemical-chemical redox cycling

ABSTRACT

An ultrasensitive electrochemical biosensor for microRNA (miRNA) is developed based on tungsten oxide-graphene composites coupling with catalyzed hairpin assembly target recycling and enzyme signal amplification. WO_3-Gr is prepared by a simple hydrothermal method and then coupled with gold nanoparticles to act as a sensing platform. The thiol-terminated capture probe H1 is immobilized on electrode through Au–S interaction. In the presence of target miRNA, H1 opens its hairpin structure by hybridization with target miRNA. This hybridization can be displaced from the structure by another stable biotinylated hairpin DNA (H2), and target miRNA is released back to the sample solution for next cycle. Thus, a large amount of H1-H2 duplex is produced after the cyclic process. At this point, a lot of signal indicators streptavidin-conjugated alkaline phosphatase (SA-ALP) are immobilized on the electrode by the specific binding of avidin-biotin. Then, thousands of ascorbic acid, which is the enzymatic product of ALP, induces the electrochemical-chemical-chemical redox cycling to produce a strongly electrochemical response in the presence of ferrocene methanol and tris (2-carboxyethyl) phosphine. Under the optimal experimental conditions, the established biosensor can detect target miRNA down to 0.05 fM (S/N=3) with a linear range from 0.1 fM to 100 pM, and discriminate target miRNA from mismatched miRNA with a high selectivity.

1. Introduction

MicroRNAs (miRNAs) are a class of small non-coding RNA molecules that play critical functions in many biological processes, such as developmental regulation, proliferation, differentiation, cardiogenesis, and epigenetic inheritance (Xia et al., 2015). Recently, accumulative evidence indicates that miRNAs are highly correlated to the cancer initiation, oncogenesis, and tumor response to treatments (Liu et al., 2015; Miao et al., 2015). At present, the presence of miRNAs in serum has been clearly detected (Hong et al., 2013). Thus, miRNAs have been regarded as clinically important biomarkers for early cancer diagnostic, drug discovery targets and prognostic processes, and effective analysis of miRNA's expression is crucial for cancer diagnosis and treatment in biological samples and clinical specimens. In the past decade, many new strategies have been developed to improve the reliability of miRNA's analysis (Dong et al., 2012; Liu et al., 2014; Lin et al., 2014; Xi et al., 2014). However, electrochemical analysis of miRNAs still remains significant challenges in the sensitivity and selectivity since the low abundance of microRNAs in biological samples and the small size of these tiny microRNAs (Leshkowitz et al., 2013; Miao et al., 2015). Signal amplification by enzyme is one of the most popular strategies for developing ultrasensitive electrochemical sensors.

Graphene (GR) is a two-dimensional carbon material composed with single-layer sheets. It has been widely used in electrochemical sensor construction due to its unique electronic, optical, thermal, and mechanical properties (Huang et al., 2013; Kumar et al., 2015), especially with its ultrathin 2D planar structures, extremely high surface areas, good electrical conductivity and chemical stability, (Huang et al., 2016) which renders it as a striking substrate material (Wang et al., 2014). As a significant transition metal oxide, tungsten oxide (WO_3) has attracted considerable attentions due to their intriguing physical and chemical properties. They have been extensively applied in gasochromic, electrochromics (Wang et al., 2008), photocatalysis (Xu et al., 2016), lithium batteries (Yu et al., 2016a) and gas sensors (Cao et al., 2016) due to its advantages of low cost, nontoxicity, abundant sources and simple fabrication process. Compared with the

* Corresponding author.
E-mail address: kejinghuang@163.com (K.-J. Huang).

http://dx.doi.org/10.1016/j.bios.2016.06.057
0956-5663/

bulk materials, metal oxide in nanoscale exhibit some totally different properties and has been regarded as a promising functional material. To further enhance its performances, the effective strategy is to prepare nanoscale WO_3 with different morphologies, small size, or large specific surface area (Li et al., 2011). Recently, a great interest has focused on the preparation of WO_3 nanostructures, such as nanoparticles (Meng et al., 2015), nanowires (Fu et al., 2015), nanorods (Tong et al., 2016), nanosheets (Xu et al., 2016), nanoflowers (Yu et al., 2016a), and nanospheres (Wang et al., 2015a). Especially, WO_3 nanosheets are very fascinating in terms of good electronic and larger specific area. Different from bulk materials, 2D layered materials have shortened path lengths for ions diffusion and large exposed surface areas, which play important roles in enhancing the electrochemical performance. However, some deficiencies largely limit the application of WO_3 semiconductor materials, for example, poor electrical properties. To overcome this problem, hybrid materials that incorporation of WO_3 with good electronic conductive substrates seem imperative.

Recently, the target catalyzed hairpin assembly has attracted considerable attention miRNAs detection, in which the signal amplification is achieved by the cycling use of the target (Yu et al., 2016b; Li et al., 2016). In these strategies, two hairpin DNA probes (H1 and H2) are first rationally designed to coexist stably in solution. The target miRNA first hybridizes with H1 when the target miRNA is added. Subsequently, H2 in the solution hybridizes with H1 and liberates miRNA for the next cycle of H1-target hybridization. During this process, each strand of target miRNA can hybridize with a large number of signal probes, leading to a considerably high signal gain. The coupling target-catalyzed hairpin assembly with electrochemical technique can offer attractive advantages, such as rapid detection, low background, high sensitivity and selectivity.

Inspired by these, WO_3-Gr hybrid materials were synthesized through a simple hydrothermal method and an ultrasensitive electrochemical sensor was then designed for detecting miRNA based on WO_3-Gr composites coupling with CHA target recycling and enzyme signal amplification. WO_3-Gr composites and gold AuNPs were used to modify glassy carbon electrode (GCE) for the immobilization of thiol-terminated capture probe H1 by Au-S bond. H1 would open its hairpin structure by hybridization with target miRNA. The hybridization of target miRNA with H1 could be displaced from the structure by another stable biotinylated hairpin DNA (H2). Target miRNA was then released for initiating next cycle and a large amount of H1-H2 duplex was produced after the cyclic process. At this point, a large number of signal indicators SA-ALP were adsorbed on the modified electrode by the specific binding of avidin-biotin. Finally, thousands of ascorbic acid (AA), which was the enzymatic product of ALP, induced the electrochemical-chemical-chemical (ECC) redox cycling to produce a strongly electrochemical response in the presence of ferrocene methanol (FcM) and tris (2-carboxyethyl) phosphine (TCEP). The as-prepared WO_3-Gr composites displayed large effective surface area and good electro-conductivity. This allowed more biomolecules (capture probe H1) to be immobilized at the electrode surface, which reduced the distance for electron transfer and ion diffusion paths between the capture probe and nanomaterials. As a result, the charge transfer to the electrodes became easier. In addition, the strong interactions between capture probe and electrode surface enhanced the surface density of the immobilized analytes, which therefore leaded to a low detection limit. This assay effectively combined WO_3-Gr composites, CHA target recycling and enzyme signal amplification and ECC redox cycling signal amplification, which led to very low detection limit for target miRNA.

2. Experimental

2.1. Reagents and materials

Graphite powder, $Na_2WO_4 \cdot 2H_2O$, $H_2C_2O_4$, hydrazine solution (50 wt%), and chloroauric acid ($HAuCl_4 \cdot 3H_2O$) were obtained from Aladdin Chemicals Co. Ltd. (Shanghai, China). Tris (carboxyethyl) phosphine (TCEP), diethylpyrocarbonate 6-mercaptohexanol (MCH), EDTA, streptavidin-conjugated alkaline phosphatase (SA-ALP), and tris-(hydroxymethyl) aminomethane hydrochloride (Tris–HCl) were purchased from Sigma-Aldrich (Shanghai, China). The water used in the experiments was obtained from a water purification system ($\geq$ 18 MΩ, Milli-Q, Millipore). The miRNAs sequence and DNA sequences were synthesized by Shanghai Sangon Biological Engineering Technology Co. Ltd. (Shanghai, China) and their sequences were as follows:

Capture probe H1:	5′-SH-TTTTCAACATCAGTCTGATAAGCTACCATGTG TAGATAGCTTATCGATACTCAGACTGATGTTGA-3′
Hairpin DNA H2:	5′-Biotin-CCATGTATCGATAAGCTATCTACACATGGT AGCTTATCAGACTGATG-3′
MiRNA-21:	5′-UAGCUUAUCAGACUGAUGUUGA-3′
Single-base mismatch:	5′-UAGCUUAUCGGACUGAUGUUGA-3′
Three-base mismatch:	5′-UUGCUUAUCGGACUGAUCUUGA-3′
Non-complementary:	5′-GUAAGGCAUCUGACCGAAGGCA-3′

The DNA solutions were prepared using TE buffer solution (10 mM Tris–HCl, 1 mM EDTA, pH 7.4), The miRNAs stock solutions were prepared daily with diethylpyrocarbonate-treated water in an RNase-free environment. The stock solution of FcM and TCEP were prepared with Tris buffer solution (10 mM, pH 8.0).

2.2. Apparatus

All electrochemical measurements were performed on an EC550 electrochemical workstation (Wuhan, Gaoss Union, China) except electrochemical impedance spectroscopy (EIS) measurements were carried out on a RST5200F electrochemical workstation (Zhengzhou Shi Rui Si Instrument, China) with a conventional three-electrode system composed of a platinum wire as auxiliary electrode, a saturated calomel electrode (SCE) as reference electrode and a 3-mm diameter GCE as working electrode. Nanostructures were characterized by a JEM 2100 transmission electron microscope (TEM, JEOL, Tokyo, Japan) and a Hitachi S-4800 scanning electron microscope (SEM, Tokyo, Japan). X-ray diffraction (XRD) pattern was operated on a model D/max-rA diffractometer (Rigaku, Japan). Raman spectra were recorded at ambient temperature on a Renishaw Raman system model 1000 spectrometer (Gloucestershire, UK).

2.3. Synthesis of grapheme oxide-tungsten oxide-graphene composites

The synthesis of WO_3-Gr composite was performed by using a one-step hydrothermal process. The graphene oxide (GO) was first prepared by the modified Hummers' method. Then, 0.5 g $Na_2WO_4 \cdot 2H_2O$, 2.0 g GO and certain amount of $H_2C_2O_4$ were dissolved in 70 mL of distilled water. Subsequently, 10 mL

hydrazine solution was added and stirred for 60 min to form a transparent solution. After that, 3.0 M HCl was added into the mixture gradually until the pH was 1.5, which resulting in a yellow precipitate. Then, the above mixture was transferred into a Teflon-lined stainless steel of 100 mL capacity and heated in an oven at 160 °C for 24 h. The products were harvested by centrifugation and dried at 60 °C for 12 h after washing by distilled water and absolute ethanol several times. For comparison, pure WO_3 were also prepared by the same method in the absence of GO.

2.4. Preparation of biosensor and electrochemical measurements

Prior to use, H1 and H2 sample were heated to 95 °C for 5 min and then slowly cooling to room temperature. For electrode preparation, 1.0 mg WO_3-Gr nanocomposites were dispersed in 1 mL water with ultrasonication for 20 min to get homogenous suspension (1 mg mL^{-1}). The bare GCE was polished sequentially with 0.3 and 0.05 μm alumina slurries, washed ultrasonically with water and ethanol and then dried with nitrogen gas. The WO_3-Gr composites modified electrode was prepared by applied 6.0 μL suspension onto the cleaned GCE and dried in the air. For assembling the capture probe H1, the AuNPs was electrodeposited on WO_3-Gr/GCE from a PBS (pH 7.0) solution containing 0.1% $HAuCl_4$ at a constant potential of −0.2 V for 50 s. After that, 8 μL of 1 nM H1 solution was dropped onto the AuNPs/WO_3–Gr/GCE and allowed to react overnight, and H1 was immobilized on the electrode by the formation of Au–S bond. After thoroughly washed with water, 8 μL BSA (1%) and 1 mM MCH were dropped on the probe H1/AuNPs/WO_3–Gr/GCE and incubated for 30 min to eliminate nonspecific adsorption. Again, the electrode was rinsed with water, and 8 μL of mixture containing different concentrations of target miRNA and H2 (T-H2) was added on H1/AuNPs/WO_3–Gr/GCE and incubated at 37 °C for 90 min. After the electrode was rinsed with water, 6 μL 0.1 mg mL^{-1} SA–ALP was then dropped on the modified electrode and incubated for 35 min. Thereafter, the resulting electrode was incubated in 5 mL of Tris buffer solution (10 mM, pH 8.0) containing 0.5 mM AAP and 1 mM $MgCl_2$ for 30 min. The resulting electrode was rinsed with water and used for electrochemical measurements.

For miRNA sensing, cyclic voltammetry (CV) was carried out in 0.1 M PBS (pH 7.0) containing 10 mmol L^{-1} $[Fe(CN)_6]^{3-/4-}$ and 0.1 mol L^{-1} KCl solution between a potential window of −0.2 V and 0.6 V with a scan rate of 100 mV s^{-1}. EIS measurements were performed in 0.1 M PBS (pH 7.0) containing 5.0 mmol L^{-1} $[Fe(CN)_6]^{3-/4-}$ and 0.1 mol L^{-1} KCl solution, with the AC voltage amplitude of 5 mV, the voltage frequencies from 100 kHz to 0.1 Hz and the applied potential of 0.2 V. The DPV measurements were conducted in the potential region from −0.4 V to 0.2 V (vs. SCE) in Tris buffer solution containing 5 mM TCEP and 2 mM FcM using a pulse amplitude of 50 mV, pulse width of 50 ms and pulse period of 0.2 s

3. Results and discussion

3.1. Design principle of the biosensor

The principle of miRNA biosensor fabrication is illustrated in Scheme 1. Two hairpin DNA segments (H1 and H2) are employed in CHA process. H1 can not automatically hybridize with H2 in absence of target. Firstly, the thiol-modified H1 is immobilized on the AuNPs/WO_3-Gr/GCE through Au–S bond. The large specific surface area and good conductivity of AuNPs/WO_3-Gr hybrid not only can immobilize more H1 but also accelerate electron transfer. Then, BSA and MCH are dropped on the electrode to eliminate nonspecific adsorption. Whereafter, the introduction of target miRNA can hybridize with H1 to form dsDNA. In the presence of H2, the binding of H1 with H2 emerges through a branch migration process (Zhang et al., 2012). Because H1–H2 duplex is longer and more stable than H1–target miRNA hybrids, the H2 will replace and liberate the target miRNA when it hybridizes with H1. The released target miRNA will come back to solution for the next hybridization cycle with H2. Thus, each target miRNA can undergo

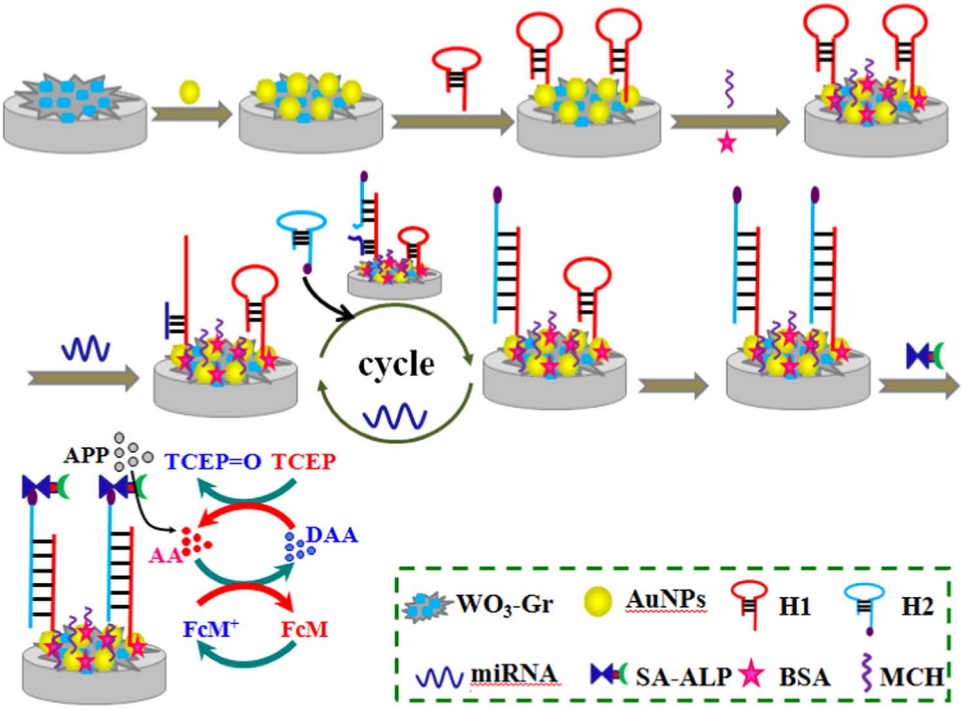

Scheme 1. Schematic illustration of the biosensor detection miRNA based on CHA target miRNA recycling and signal amplification of ALP coupled with ECC redox cycling.

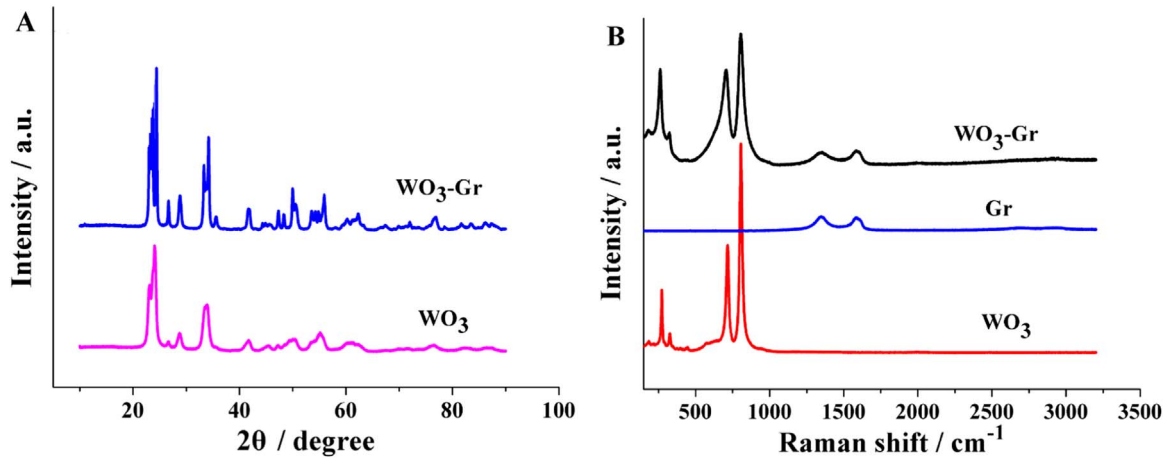

Fig. 1. XRD patterns (A) and Raman spectra (B) of WO_3 and WO_3-Gr composites.

many cycles. The biotin tags in the end of H2 allow SA-ALP to be attached through the streptavidin–biotin interaction. SA-ALP on the electrode will catalyze the production of large amounts of AA, triggering the ECC redox cycling to produce a strongly electrochemical response. Thus, the sensitivity of the as-prepared miRNA biosensor can be conspicuously enhanced by using WO_3-Gr hybrid, CHA target recycling, and SA-ALP coupling with ECC redox cycling as signal amplification protocol.

3.2. Characterization of as-prepared materials

The XRD patterns of the as-prepared WO_3 nanosheets and WO_3-Gr composites are shown in Fig. 1A. All the observed diffraction peaks in the XRD pattern are sharp and indexes to the hexagonal WO_3 and in accordance well with the standard data file (JCPDS file no. 75-2187), indicating the products with high crystallization. However, no obvious diffraction peaks of graphene are observed in the XRD pattern of WO_3-Gr composites due to the small amount of graphene in products and less atomic number of carbon. This result has been documented in the previous literature (Shao et al., 2013).

Further insights of the structural and electronic properties of products were obtained from Raman spectrum. Fig. 1B shows the Raman spectra of WO_3 nanosheets, Gr and WO_3-Gr composites. The Raman spectrum of Gr shows two distinctive peaks at about 1350 and 1591 cm^{-1}, which are assigned to the D and G band of Gr, respectively. As for WO_3-Gr, sharp peaks for WO_3 and low-intensity peaks for Gr are observed cleanly. Sharp peaks located at about 257 and 325 cm^{-1} are attributed to the W-O-W bending mode, and peaks at about 706 and 807 cm^{-1} are attributed to the O-W-O stretching mode. Peaks at around 1351 and 1592 cm^{-1} are assigned to the D and G band of Gr, respectively, which verifies the existence of Gr in composites.

The morphology of the as-obtained WO_3 nanosheets, Gr and WO_3-Gr composites were characterized with SEM and TEM. The SEM images of WO_3 nanosheets are shown in Fig. 2A. It is clearly observed that WO_3 shows quadrate nanosheets with high uniformity. Fig. 2B reveals that Gr is 2D nanosheet structure with the typical crumpled and wrinkled. As shown in Fig. 2C and D, it shows WO_3 nanosheets distribute well on the Gr 2D skeleton, exhibiting the well behaved assembly process. The cumulate layered sheets architecture is beneficial to enlarge specific surface area of the WO_3-Gr composite, which is helpful to load more H1 and therefore leads to enhanced electrochemical performance. Fig. 2F indicates Gr is layered structure with crinkles. As shown in Fig. 2F, WO_3 shows its typical nanosheets. From Fig. 2G, it can be observe obviously that WO_3 nanosheets are supported on the Gr surface. The HRTEM image of the WO_3-Gr composites is shown in Fig. 2H. It can be seen clearly that WO_3 nanosheets provides many pores and channels, and the spacing of the lattice fringes is about 0.316 nm.

3.3. Electrochemical characterization

CV was used to characterize different modified electrodes (Fig. 3). As shown in Fig. 3A, the bare GCE displays a couple well-defined redox peaks in $[Fe(CN)_6]^{3-/4-}$ solution (curve a). The presence of Gr on the GCE yields an increase peak current (curve b) due to the good conductor of Gr. The peak currents apparently enhance when WO_3-Gr modified on the GCE because of its large specific surface area and good conductivity (curve c). The current respond reaches the maximum when AuNPs are further modified on the WO_3-Gr/GCE due to the conductive AuNPs can accelerate the electron transfer rate (curve d). However, as shown in Fig. 3B, the current responses decrease greatly when H1 is applied on above electrode, accounting for the fact that H1 can hinder the diffusion of ferricyanide toward the electrode surface (curve e). The redox currents gradually decrease after the electrode reacted with BSA and MCH, (curves f and g) due to the fact that the protein and negative charges of DNA insulate the conductive support and the electron transfer become more difficult. Additionally, the peak currents further decrease after incubating the mixture of T-H2 (curve h). This is attributed to the successful CHA process and more negatively charged DNA strands loaded on the electrode surface, inhibiting the diffusion of redox probe. The CV results suggested the successful construction of the biosensor.

EIS is one important tool for probing the features of surface-modified electrodes. In the impedance spectra, the increase in the diameter of the semicircle indicates the enhancement in the interfacial electron transfer resistance (Ret). Fig. 3C showed the characteristic EIS corresponding to the stepwise modification processes. The bare GCE displays a largest Ret value (curve a). When Gr (curve b) and WO_3-Gr (curve c) are assembled on the GCE, the Ret become smaller than the bare GCE due to its good conductivity. However, the Ret value of WO_3-Gr composite shows lower value, indicating the better conductivity of WO_3-Gr. After AuNPs are further applied on WO_3-Gr/GCE, the Ret greatly decreases and exhibits almost a line (curve d), which is ascribed to the synergistic effect of AuNPs and WO_3-Gr, indicating rapid electron transfer. As shown in Fig. 3D, the Ret value obviously increases after H1 is applied to the electrode surface due to its hindering the electron transfer (curve e). When MCH and BSA (curves f, g) immobilized on the electrode, the Ret value further increases, which may originate from the protein and negative

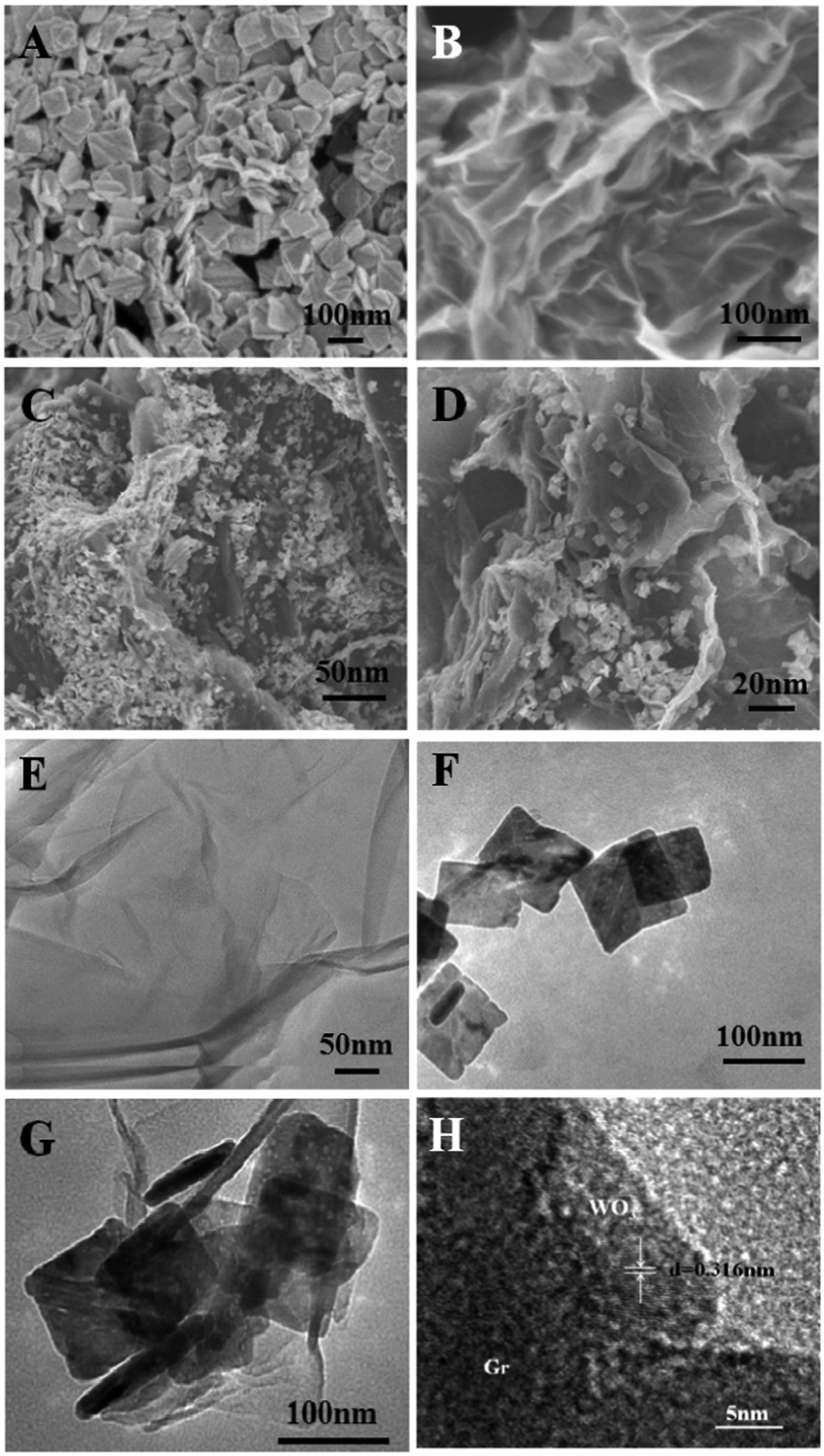

Fig. 2. SEM images of WO_3 (A), Gr (B) and WO_3-Gr composites (C, D); TEM images of Gr (E), WO_3 (F), and WO_3-Gr composites (G); HRTEM image of WO_3-Gr composites (H).

charges DNA sequences blocking the electrode surface. After incubating the mixture of T-H2 (curve h), the Ret of electrode apparently increases due to more negatively charged DNA strands are loaded. The EIS results are consistent with CV.

The effective surface areas of GCE and AuNPs/WO_3-Gr/GCE were compared by chronocoulometry in 0.1 mM $K_3[Fe(CN)_6]$ solution containing 1.0 M KCl, where the standard diffusion coefficient (D_0) of $K_3[Fe(CN)_6]$ at 25 °C is 7.6×10^{-6} cm^2 s^{-1}. The effective surface area (A) of electrodes is calculated according to the following equation:

$$Q=2nFAcD^{1/2}t^{1/2}/\pi^{1/2}+Q_{dl}+Q_{ads} \quad (1)$$

where n is the number of electron transferred, F (C mol^{-1}) is the Faraday constant, A (cm^2) is the area of the electrode, c (mol cm^{-3}) is the concentration of substrate, D (cm^2 s^{-1}) is the diffusion coefficient, Q_{dl} (C) is the double layer charge and Q_{ads} (C) is the

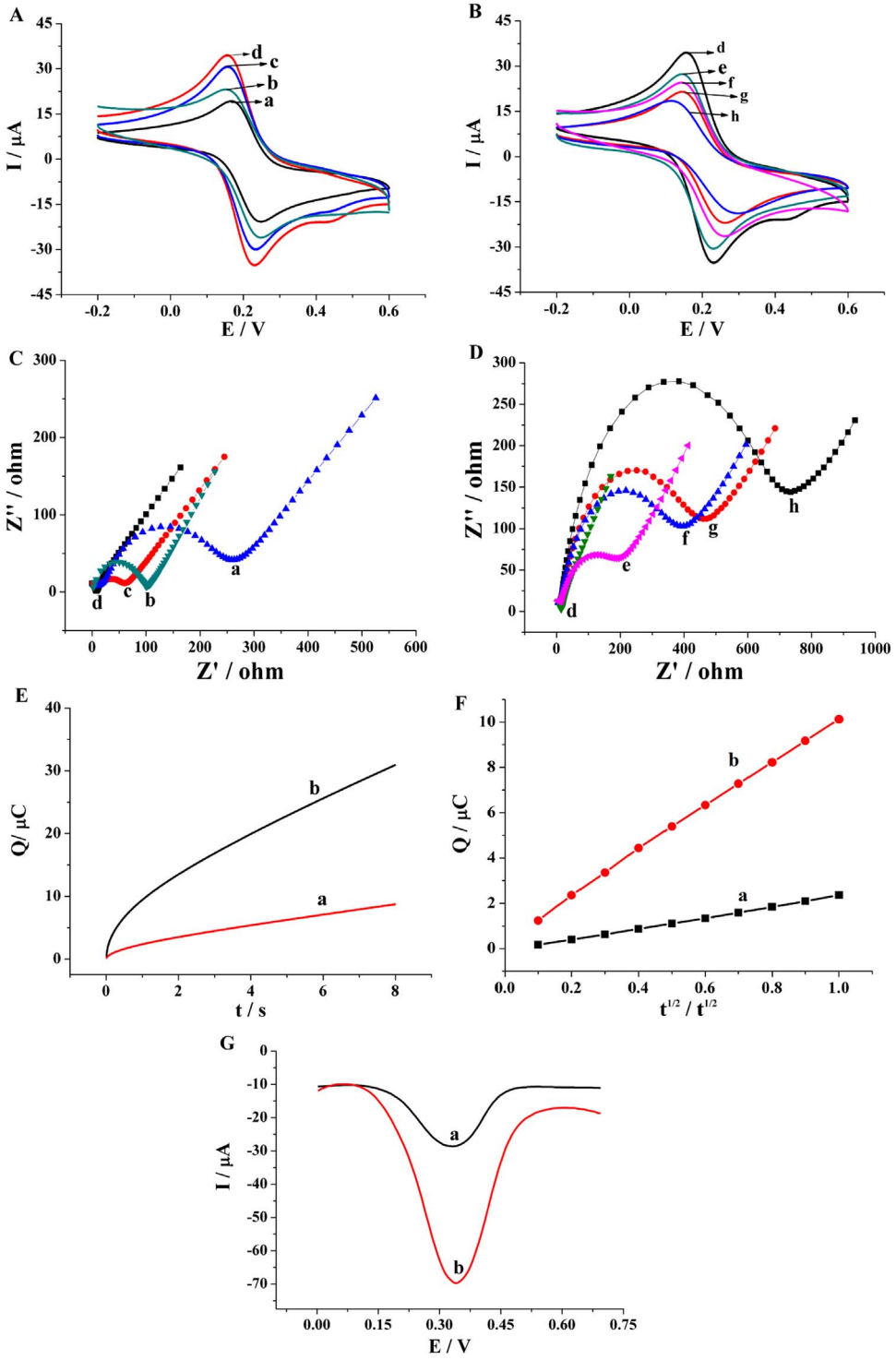

Fig. 3. CVs (A, B) and EIS (C, D) of bare GCE (a), Gr/GCE (b), WO_3-Gr/GCE (c) AuNPs/WO_3-Gr/GCE (d), H1/AuNPs/WO_3-Gr/GCE/GCE (e), BSA/H1/AuNPs/ WO_3-Gr/GCE/GCE (f), MCH/BSA/H1/AuNPs/WO_3-Gr/GCE/GCE (g), T-H2/MCH/ BSA/AuNPs/WO_3-Gr/GCE/GCE (h), CV experiments were conducted in 0.1 M PBS solution containing 1.0 mM $[Fe(CN)_6]^{3-/4-}$ and 0.1 M KCl; (E) Plot of Q-t curves of the bare GCE (a) and AuNPs/WO_3-Gr/GCE (b) in 0.1 mM $K_3[Fe(CN)_6]$ containing 1.0 M KCl; (F) plot of Q-$t^{1/2}$ curves on GCE (a) and AuNPs/WO_3-Gr/GCE (b); (G) DPVs of AAP/SA-ALP/T-H2/MCH/BSA/H1/AuNPs/GCE(a) and AAP/SA-ALP/T-H2/MCH/BSA/H1/AuNPs/WO_3-Gr/GCE (b) in 10 mM Tri buffer solution (8.0) containing 5 mM TCEP and 2 mM FCM.

adsorption charge and other symbols have their usual significances. According to the results shown in Fig. 3E and F, A is calculated to be 0.018 cm^2 and 0.082 cm^2 for bare GCE and AuNPs/WO_3-Gr/GCE, respectively. The results indicated that the effective surface area of the electrode increased greatly after modification with AuNPs/WO_3-Gr film.

Fig. 3G shows the signal-amplification effect of the as-prepared material. Current signal greatly increases when the WO_3-Gr composite is employed in the sensor construction (curve b). The corresponding signal gain in the presence of WO_3-Gr composite is about 214.3% for that in the absence of WO_3-Gr composites (curve a), indicating the WO_3-Gr composite is helpful to enhance detection sensitivity.

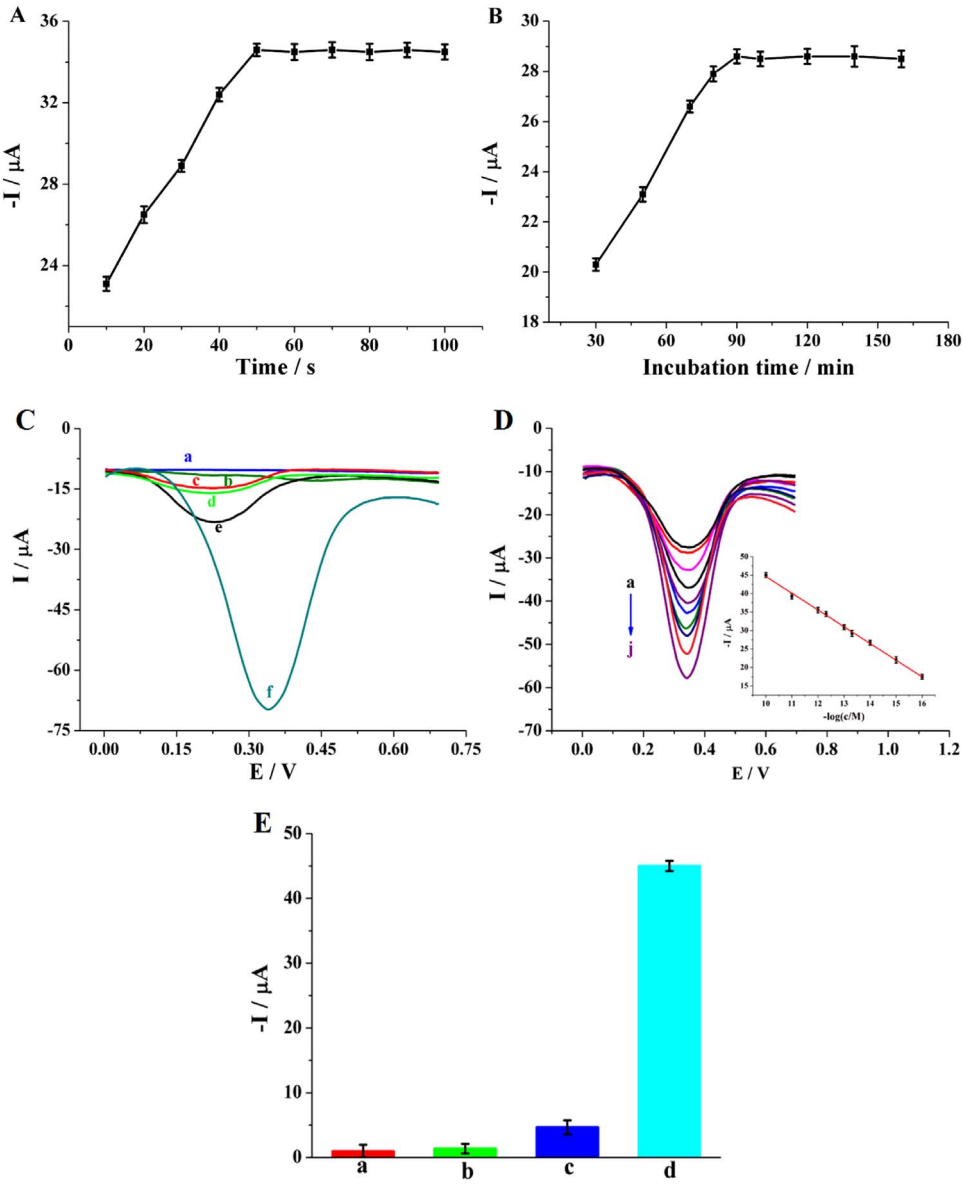

Fig. 4. Effects of deposition time of AuNPs (A), incubation time of H1 and target miRNA/H2 (B); (C) DPVs curves responding of the biosensor in different substrate solutions: AAP (a); AAP/TCEP (b); FcM (c); TCEP/FcM (d); AAP/FcM (e); and AAP/TCEP/FcM (f); (D) DPVs of various target miRNA concentrations (from a to i): 0, 1.0×10^{-10}, 1.0×10^{-11}, 1.0×10^{-12}, 5.0×10^{-12}, 1.0×10^{-13}, 5.0×10^{-13}, 1.0×10^{-14}, 1.0×10^{-15}, 1.0×10^{-16} mol L^{-1}, respectively. Inset: the calibration plots of the DPV current versus the logarithm concentration of target miRNA. Error bars show the standard deviations of measurements taken from three independent experiments; (E) selectivity of the sensor hybridized to different miRNA sequences: non-complementary sequence (a), three-based mismatch sequence (b), single-based mismatch sequence (c), and target miRNA (d).

3.4. Optimization of experimental conditions

To obtain good analytical performance, several experimental conditions were optimized. The effect of deposition time of AuNPs was tested in the range of 10–80 s (Fig. 4A). The highest current response is obtained at a deposition time of 50 s. So 50 s of deposition time was used.

The effect of the incubation time between H1 and T-H2 on the DPV response was evaluated. As shown in Fig. 4B, the peak current increases rapidly when the reaction time ranges from 20 to 90 min, and almost remains stable after 90 min, suggesting that the hybridization reaction is completed. Thus, 90 min of incubation time was used.

3.5. Signal amplification of detection system

In this work, the detection system was based on SA-ALP catalysis of the oxidation substrate of AAP, TCEP and FCM. As shown Fig. 4C, the DPV of the biosensor in different substrate solutions was tested. No redox response was observed in the solutions of AAP (curve a) and AAP/TCEP (curve b), indicating that the insulating DNA/MCH self-assembled monolayers impeded the electro-oxidation of AA. In the FcM system, the large peak current is observed (curves c and e) due to the generated AA causing a significant increase in the anodic current of FcM. The electrode reaction is characteristic of an electrochemical–chemical (EC) reaction mechanism, demonstrating that FcM mediates the electron transfer between AA and electrode. Furthermore, the presence of TCEP induces a more significant increase in the peak current (curve f). The result can be attributed to the regeneration of AA from its oxidized product by TCEP. However, TCEP itself does not induce a change in the anodic current of FcM (curves d). These results indicate that the EC reaction between FcM and AA is promoted by the chemical–chemical (CC) reaction between AA and TCEP. Thus, EEC redox cycling reaction can greatly improve the electrochemical signal.

Table 1
Comparison between the proposed assay and other reported method for miRNA detection.

Methods	Detection time (min)	Linear range (pM)	LOD (fM)	References
Fluorescence method based on gold-nanorod functionalized polydiacetylene microtube waveguide	120	50–1000	10	(Zhu, 2016)
Electrochemical sensor based on DNA concatamers	120	0.0001–100	0.1	(Hong et al., 2013)
Electrochemical sensor based on poly (U) polymerase mediated isothermal signal amplification	120	0.01–1	1.7	(Zhou et al., 2016)
Electrochemical detection based on AuNPs/ALP/redox cycling	120	0.001–5	3	(Liu et al., 2014)
Fluorescence detection based on hybridization chain reaction and catalytic hairpin assembly	120	0.001–100	0.3	(Wei et al., 2016)
Electrochemical sensor using methylene blue as redox indicator	60	0.1–500	84.3	(Rafiee-Pour et al., 2016)
Electrochemical Immunosensing based on IgG-ALP/AuNPs	150	0.0005–0.5	0.4	(Wang et al., 2015b)
AuNPs/WO_3Gr /GCE	90	0.0001–100	0.05	This work

3.6. Analytical performance of designed biosensor

Under the optimal conditions, various concentrations of target miRNA were detected. Fig. 4C shows the peak current increases with the increasing concentration of target miRNA. There was a good linear relationship between the peak current and the logarithm of the target DNA concentration in the ranged of 0.1 fM–100 pM. The linear calibration equation was $I(\mu A) = -4.98 \log(c/M) - 81.17$ (I is the peak current and c is the concentration of target miRNA) with a correlation coefficient (R) of 0.998. The detection limit was 5.0×10^{-17} M (S/N=3). The analytical performances of different assays are compared in Table 1. The proposed assay exhibits the lowest detection limit, the widest detection range and comparable detection time (Liu et al., 2014; Zhu et al., 2016; Wang et al., 2015b; Zhou et al., 2016; Wei et al., 2016; Hong et al., 2013; Rafiee-Pour et al., 2016).

The analytical applicability of the proposed miRNA-21 biosensor was evaluated by the standard addition method. The proposed miRNA-21 biosensor was used to determine the miRNA-21 in the total RNA samples and the recovery (addition of miRNA-21, 10 pM; $n=3$) is 104.4% with a RSD of 4.8%. The acceptable recovery and RSD suggest that the proposed biosensor has potential application in complex miRNA samples.

3.7. Selectivity, stability and reproducibility

The selectivity of proposed method was investigated by measuring the peak current variation of the biosensor with different miRNA sequences including non-complementary sequence, three-based mismatch sequence, one-based mismatch sequence and the complementary sequence. As shown in Fig. 4D, the higher peak current is obtained for the complementary sequence than the other sequences. The peak current of non-complementary sequence and three-based mismatch sequence is negligible, indicating that both miRNAs did not hybridize with H1. In the case of single-base mismatched sequence, the peak current is only 10.33% of that of complementary sequence. These results indicate that the proposed biosensor has high selectivity for target miRNAs detection.

The stability of the miRNA biosensor was investigated. The T-H2/MCH/BSA/H1/AuNPs/WO_3-Gr/GCE was incubated in ultrapure water, TE buffer, Tris buffer and washing buffer at 30 °C for 6 h, respectively. After that, 6 μL 0.1 mg mL^{-1} SA-ALP was dropped and incubated for 35 min. Thereafter, the resulting sensing electrode was incubated with 5 mL of Tris buffer solution (10 mM, pH 8.0) in the presence of 0.5 mM AAP and 1 mM $MgCl_2$ for 30 min, Then the T-H2/MCH/BSA/H1/AuNPs/WO_3-Gr/GCE was tested in Tris buffer solution containing 5 mM TCEP and 2 mM FcM by DPV according to the procedure. The results showed that the incubated electrode had almost the same behavior as the unincubated electrode. The long-term stability of proposed biosensor was also investigated. When the biosensor was stored at 4 °C for 10 days, it retained 95.6% of its initial current response, indicating good stability.

The reproducibility of any biosensing platform is extremely important in detecting miRNA. Herein, the reproducibility of the miRNA biosensor was also investigated. Nine parallel-made T-H2/MCH/BSA/H1/AuNPs/WO_3-Gr/GCEs were used to detect 1×10^{-9} mol L^{-1} target miRNA, respectively. The relative standard deviation (RSD) of the biosensor was 6.4%, indicating a satisfactory reproducibility.

3.8. Real samples analysis

To evaluate the applicability of proposed biosensor, 5 human serum samples from newly diagnosed breast cancer patients were tested. Human serum samples of breast cancer patients (confirmed by pathological examinations) were obtained from Xinyang Central Hospital (Xinyang, China). Signed informed consent was obtained from each patient participating in the study before surgery. Before use, serum samples were heated at 95 °C for 10 min. As references, expression levels of the serum miRNA-21 were simultaneously quantified by a commercial qRT-PCR kit. The analytical results are shown in Table S1. The results obtained with the biosensors are in good agreement with those obtained by qRT-PCR, confirming the practical value of developed biosensor.

4. Conclusion

In summary, we report highly sensitive electrochemical sensor for miRNA detection based on WO_3-Gr composites coupling with CHA target recycling and enzyme signal amplification. This strategy had several excellent features. First, the large specific surface area of WO_3-Gr composites provided a promising sensing platform. Second, the target miRNAs hybridized with H1 can be replaced by H2 on electrode surface, releasing miRNAs back to the sample solution for next recycling. Third, the sensing system showed high selectivity due to CHA target miRNA recycling. Finally, the application of signal amplification of enzyme plus EEC redox cycling reaction leaded to a remarkable lower detection limit (0.05 fM). The high sensitivity and selectivity of proposed method indicated that our work would be valuable for quantifying miRNAs in clinical diagnostic and prognostic.

Acknowledgments

This work was supported by the National Natural Science Foundation of China (U1304214 and 21475115), Program for University Innovative Research Team of Henan (15IRTSTHN001),

Henan Provincial Science and Technology Innovation Team (C20150026), Nanhu Scholars Program of XYNU and Science and Technology Major Project of Henan Province (141100310600).

Appendix A. Supplementary material

Supplementary data associated with this article can be found in the online version at http://dx.doi.org/10.1016/j.bios.2016.06.057.

References

Cao, S.S., Zhao, C., Han, T., Peng, L.L., 2016. Mater. Lett. 169, 17–20.
Dong, H., Zhang, J., Ju, H., Lu, H., Wang, S., Jin, S., Hao, K., Du, H., Zhang, X., 2012. Anal. Chem. 84, 4587–4593.
Fu, L., Cai, W., Wang, A., Zheng, Y., 2015. Mater. Lett. 142, 201–203.
Hong, C.Y., Chen, X., Liu, T., Li, J., Yang, H.H., Chen, J.H., Chen, G.N., 2013. Biosens. Bioelectron. 50, 132–136.
Huang, K.J., Shuai, H.L., Zhang, J.Z., 2016. Biosens. Bioelectron. 77, 69–75.
Huang, K.J., Wang, L., Liu, Y.J., Liu, Y.M., Wang, H.B., Gan, T., Wang, L.L., 2013. Int. J. Hydrog. Energy 38, 14027–14034.
Kumar, S., Ahlawat, W., Kumar, R., Dilbaghi, N., 2015. Biosens. Bioelectron. 70, 498–503.
Leshkowitz, D., Horn-Saban, S., Parmet, Y., Feldmesser, E., 2013. RNA 19, 527–538.
Li, C.C., Yin, X.M., Li, Q.H., et al., 2011. CrystEngComm 13, 1557–1563.
Li, X.M., Cheng, W., Li, D.D., Wu, J.L., Ding, X.J., Cheng, Q., Ding, S.J., 2016. Biosens. Bioelectron. 80, 98–104.
Lin, M., Wen, Y., Li, L., Pei, H., Liu, G., Song, H., Zuo, X., Fan, C., Huang, Q., 2014. Anal. Chem. 86, 2285–2288.
Liu, L., Xia, N., Liu, H., Kang, X., Liu, X., Xue, C., He, X., 2014. Biosens. Bioelectron. 53, 399–405.
Liu, L., Gao, Y.P., Liu, H.P., Xia, N., 2015. Sens. Actuators B 208, 137–142.
Meng, Z., Fujii, A., Hashishin, T., Wada, N., Sanada, T., Tamaki, J., Kojima, K., Haneoka, H., Suzuki, T., 2015. J. Mater. Chem. C 3, 1134–1141.
Miao, P., Wang, B., Yu, Z., Zhao, J., Tang, Y., 2015. Biosens. Bioelectron. 63, 365–370.
Rafiee-Pour, H.A., Behpour, M., Keshavarz, M., 2016. Biosens. Bioelectron. 77, 202–207.
Shao, D.L., Yu, M.P., Lian, J., Sawyer, S., 2013. Nanotechnology 24, 1–5.
Tong, P.V., Hoa, N.D., Van Duy, N., Thanh Le, D.T., Van Hieu, N., 2016. Sens. Actuators B 223, 453–460.
Wang, C., Feng, C., Wang, M., Li, X., Cheng, P., Zhang, H., Sun, Y., Sun, P., Lu, G., 2015a. RSC Adv. 5, 29698–29703.
Wang, J.M., Khoo, E., Lee, P.S., Ma, J., 2008. J. Phys. Chem. C 112, 14306–14312.
Wang, M., Li, B.C., Zhou, Q., Yin, H.S., Zhou, Y.L., Ai, S.Y., 2015b. Electrochim. Acta 165, 130–135.
Wang, Y.H., Xu, J.M., Ma, C., Li, S., Yu, J.H., Ge, S.G., Yan, M., 2014. J. Mater. Chem. B 2, 3462–3468.
Wei, Y.L., Zhou, W.J., Li, X., Chai, Y.Q., Yuan, R., Xiang, Y., 2016. Biosens. Bioelectron. 77, 416–420.
Xi, Q., Zhou, D.M., Kan, Y.Y., Ge, J., Wu, Z.K., Yu, R.Q., Jiang, J.H., 2014. Anal. Chem. 86, 1361–1365.
Xia, N., Zhang, Y.J., Wei, X., Huang, Y.P., Liu, L., 2015. Anal. Chim. Acta 878, 95–101.
Xu, H., Liu, L., Song, Y.H., Huang, L.T.Y., Li, Y.P., Chen, Z.G., Zhang, Q., Li, H.M., 2016. J. Alloy. Compd. 660, 48–54.
Yu, Y.C., Zeng, W., Zhang, H., 2016a. Mater. Lett. 171, 162–165.
Yu, Y.Q., Wang, J.P., Zhao, M., Hong, L.R., Chai, Y.Q., Yuan, R., Zhuo, Y., 2016b. Biosens. Bioelectron. 77, 442–450.
Zhang, D.Y., Chen, S.X., Yin, P., 2012. Nat. Chem. 4, 208–214.
Zhou, Y.L., Yin, H.S., Li, J., Li, B.C., Li, X., Ai, S.Y., Zhang, X.S., 2016. Biosens. Bioelectron. 79, 79–85.
Zhu, Y., Qiu, D., Yang, G., Wang, M.Q., Zhang, Q.J., Wang, P., Ming, H., Zhang, D.G., Yu, Y., Zou, G., Badugu, R., Lakowicz, J.R., 2016. Biosens. Bioelectron. 85, 198–204.